Room-temperature weak collinear ferrimagnet with symmetry-driven large intrinsic magneto-optic signatures

F. Johnson [1,*] J. Zázvorka [2,*] L. Beran,[2] D. Boldrin [1,3] L. F. Cohen [1,†] J. Zemen [4] and M. Veis [2,‡]

[1]*Department of Physics, Imperial College London, London SW7 2AZ, United Kingdom*

[2]*Charles University, Faculty of Mathematics and Physics, Ke Karlovu 5, Prague 121 16, Czech Republic*

[3]*SUPA, School of Physics and Astronomy, University of Glasgow, Glasgow G12 8QQ, United Kingdom*

[4]*Czech Technical University in Prague, Faculty of Electrical Engineering, Technická 2, 166 27 Prague, Czech Republic*

(Received 4 July 2022; revised 30 September 2022; accepted 14 November 2022; published 9 January 2023)

Here we present a magnetic thin film with a weak ferrimagnetic (FIM) phase above the Néel temperature ($T_N = 240$ K) and a noncollinear antiferromagnetic (AFM) phase below, exhibiting a small net magnetization due to strain-associated canting of the magnetic moments. A long-range ordered FIM phase has been predicted in related materials, but without symmetry analysis. We now perform this analysis and use it to calculate the magneto-optical Kerr effect (MOKE) spectra in the AFM and FIM phases. From the good agreement between the form of the measured and predicted MOKE spectra, we propose the AFM and FIM phases share the magnetic space group $C2'/m'$ and that the symmetry-driven magneto-optic and magneto-transport properties are maximized at room temperature in the FIM phase due to the nonzero intrinsic Berry phase contribution present in these materials. A room temperature FIM with large optical and transport signatures, as well as sensitivity to lattice strain and magnetic field, has useful prospects for high-speed spintronic applications.

DOI: 10.1103/PhysRevB.107.014404

I. INTRODUCTION

Antiferromagnets (AFMs) have been of renewed focus for spintronic applications because of the opportunity for high-speed, high-density memory and logic functions [1,2]. Certain families of AFMs have captured interest because the symmetry of their spin structure offers additional functionality. Semimetallic CuMnAs [3,4] and metallic Mn_2Au [5,6] share the property that each spin sublattice in their collinear spin structure forms inversion partners, which allows for staggered current-induced electrical switching of AFM domains via spin-orbit–induced torques. However, although writing information in AFMs has proved encouraging, reading has proved less so, with typically 0.2% anisotropic magneto-resistance reported in CuMnAs [7] and 6% in Mn_2Au [6]. Furthermore, there have been questions raised regarding the influence of anisotropic thermal gradients on the measured signals due to the high current density (see Ref. [8] and references therein).

AFMs with frustrated exchange interactions between manganese ions also offer unique opportunities for spintronic applications because of the chiral magnetic structures found in both hexagonal crystal symmetry Heuslers Mn_3X ($X =$ Sn, Ge, Gd) and cubic antiperovskite Mn_3Y [$Y =$ Pt, Ir], and Mn_3AN ($A =$ Ga, Sn, Ni) compounds [9]. In the latter case, the low-temperature noncollinear AFM spin structure in these materials can take two forms, known as Γ^{4g} and Γ^{5g}, related via a 90° rotation of the three manganese spins in the (111) plane. For the systems that support the Γ^{4g} spin arrangement, the magnetic symmetry along with Weyl points in the band structure close to the Fermi energy allow for a nonzero Berry phase curvature underpinning functional properties below the Néel temperature (T_N), such as the anomalous Hall effect (AHE) [10–16], anomalous Nernst effect [17–20], and magneto-optical Kerr effect (MOKE) [21]. The Mn_3AN materials have also been shown to support strain-sensitive piezomagnetic [22–24] or piezospintronic [25–27] properties.

The attraction of AFMs in terms of their insensitivity to external fields is also a challenge for manipulation of states. Attention has turned recently to exploiting certain classes of ferrimagnets (FIMs) that offer the advantages of speed, and density, with a small unsaturated moment close to their compensation temperature, enabling manipulation of the magnetic properties using small magnetic fields [28]. Previously, a collinear FIM phase in Mn_3GaN [29] was predicted to occur above T_N in compressively strained films, although no symmetry analysis was done. Following this, a weak magnetism in Mn_3NiN grown on $SrTiO_3$ and $BaTiO_3$ substrates above T_N was observed experimentally and attributed to this phase [30]. However, the magnetic space group of the latter could not be identified directly. Moreover, Mn_3GaN and Mn_3NiN are predicted to have different magnetic space groups in the AFM phase, suggesting a direct link between the phase predicted in Ref. [29] and the observations in Ref. [30] was unlikely.

The symmetry analysis of the FIM phase of compressively strained Mn_3NiN, analogous to the FIM phase predicted in Mn_3GaN in Ref. [29], is conducted in this work using FINDSYM software [31,32] (see table S1 in the Supplemental Material [33] for details) and is found to be magnetic space group $C2'/m'$. Using this, we determine the spectral dependence of the MOKE for a collinear FIM phase with magnetic space group $C2'/m'$ by spin density functional theory and

*These authors contributed equally to this work.
†Corresponding author: l.cohen@imperial.ac.uk
‡veis@karlov.mff.cuni.cz

linear response approximation, and compare it to experimentally measured MOKE above and below the Néel temperature on films grown on $BaTiO_3$ substrates. We observe strong qualitative agreement of the data to the theory. We show complementarity in the temperature dependence of MOKE and AHE, and demonstrate that both are maximized at room temperature.

Both intrinsic AHE and MOKE can be observed in materials without net magnetization if a fictitious magnetic field in the momentum space is present [10,14,34,35]. This field is associated with a non-vanishing Berry curvature, which is a property of the electronic structure. Within linear response theory, we can express the anomalous Hall conductivity (AHC) as an integral of the Berry curvature over the Brillouin zone [12,14]

$$\sigma_{\alpha,\beta} = \frac{-e^2}{\hbar}\int \frac{dk}{2\pi^3}\sum_{n(\text{occ.})} f[\epsilon(k)-\mu]\Omega_{n,\alpha,\beta}(k),$$

$$\Omega_{n,\alpha,\beta}(k) = -2Im\sum_{m\neq n}\frac{\langle km|v_\alpha(k)|kn\rangle\langle kn|v_\beta(k)|km\rangle}{[\epsilon_{kn}-\epsilon_{km}]^2},$$

where $f[\epsilon(k)-\mu]$ denotes the Fermi distribution function with Fermi energy indicated by μ, and ϵ_{kn} are the energy eigenvalues corresponding to occupied (unoccupied) Bloch band n, where $v_\alpha(k)$ corresponds to the velocity operator in Cartesian coordinates. $\Omega_{n,\alpha,\beta}(k)$ is the Berry curvature for given band n in the Brillouin zone.

The Kerr angle (θ_K) and ellipticity (η_K) relevant for this study (with the z-axis perpendicular to the film surface) can be calculated from the AHC as follows [36]:

$$\theta_K + i\eta_K = \frac{-\sigma_{xy}}{\sigma_{xx}\sqrt{1+i(4\pi/\omega)\sigma_{xx}}}$$

Since Berry curvature is a pseudovector defined in the Brillouin zone, the presence of AHE and MOKE in systems with time-reversal symmetry broken by the presence of local magnetic moments can be determined by analyzing the transformation properties of the Berry curvature pseudovector under all the symmetry operations of the particular system.

Unstrained Mn_3NiN with the Γ^{4g} phase (magnetic symmetry group $R\bar{3}m'$ common also to Mn_3Ir or Mn_3Pt, as confirmed by FINDSYM software [31,32]) and with spin-orbit coupling has broken mirror symmetry of the (111) plane M, in addition to the broken time-reversal symmetry T. However, the combined TM symmetry is preserved and makes the Berry curvature an even function of wavevector k [14]. After integration over the Brillouin zone, this even property of the Berry curvature makes the AHC as well as MOKE nonzero in the Γ^{4g} phase (but zero in the Γ^{5g} phase due to the invariance under the mirror symmetry transformations). In-plane biaxial strain *below* T_N induces canting of the manganese moments and lowers the symmetry to magnetic space group $C2'/m'$. This preserves the nonvanishing Berry curvature, and therefore the AHC tensor has two independent elements [37] as shown in Supplemental Material Table S1 [33].

In-plane biaxial strain *above* T_N may induce the collinear FIM phase with net magnetization along the $[-1, 1, 2]$ axis, analogous to the FIM phase predicted in Ref. [29]. Based on symmetry analysis, we predict that this novel phase should share the same magnetic space group and form of AHC as the canted Γ^{4g} phase [31,32,37]. In contrast to a typical collinear FIM system with two mutually compensating sublattices, where the MOKE signal vanishes together with net magnetization at the compensation temperature (time inversion combined with lattice translation is a symmetry operation, so the Berry curvature vanishes), the collinear FIM phase [related by a 90 ° rotation of all moments within the (111) plane to magnetic space group $Cmm'm'$ predicted in Mn_3GaN] involves three magnetic sublattices, and the magnetic space group $C2'/m'$ enables large Berry curvature despite the nearly compensated net magnetization. We note that biaxial strain applied to a closely related noncollinear system Mn_3Pt has been shown to induce a collinear AFM state above room temperature (F-phase) [38]. AHC hosted by the noncollinear phase vanishes in the collinear AFM phase [25], which contrasts with the behavior of Mn_3NiN presented here (the corresponding space groups and AHC tensors are summarized in Supplemental Material Table S1 [33]).

We complement this qualitative analysis of MOKE based on symmetry consideration with simulations of the MOKE spectra using density functional theory (DFT) and linear response theory. Details are given in the next section.

II. EXPERIMENTAL AND THEORETICAL DETAILS

A. Measurement of magnetization and AHE

One hundred–nanometer Mn_3NiN thin films were deposited on (001)-oriented single-crystal $BaTiO_3$ (BTO) and $SrTiO_3$ (STO) substrates using pulsed laser deposition from a Mn_3NiN stoichiometric target. The substrates were first heated to 400 °C and the films were then deposited in a N_2 atmosphere, pressure 5 mTorr, using a KrF excimer laser ($\lambda = 248$ nm) with a laser fluency of 0.8 J/cm^2. The films were then cooled in the N_2 atmosphere to room temperature.

Magnetization data were collected using the VSM option in a Quantum Design Physical Property Measurement System (PPMS-9T). For measurements with the field out of plane, the samples were mounted in a plastic straw with the film surface perpendicular to the applied field. For in-plane measurements, the sample was secured to a quartz paddle with GE 7031 varnish. Linear backgrounds were subtracted. Four-point probe electrical and magneto-transport data were collected using the van der Pauw technique. $\rho_{xy}(H)$ loops were measured in fields of up to 7 T, and the data were then antisymmetrized to extract the Hall component. The saturated values $\rho_{xy,\text{sat}}$ were obtained by subtracting the linear ordinary Hall component, which was found by the slope at high field.

B. Measurement of MOKE spectra

The MOKE spectra were measured using a field-cooled protocol in a broad spectral region from 1.5 to 5 eV, using a rotating analyzer setup [39] with a laser-driven xenon lamp as a white light source and a charge-coupled device spectrometer as a detector. This allows the experimental data to be collected in the polar configuration (where the magnetic field is perpendicular to the sample surface) with accuracy below 1 mdeg. The sample was measured in an optical cryostat with a static out-of-plane magnetic field of ±200 mT applied

using a permanent magnet. The direction of the magnetic field was reversed by mechanical rotation of the permanent magnet. These data were then antisymmetrized to obtain the polar Kerr angle $\theta_K = [\theta_K(200\ \text{mT}) - \theta_K(-200\ \text{mT})]/2$. This procedure ensures the resulting data are of magneto-optical origin, and removes time-reversal effects and quadratic magneto-optical contributions. The parasitic Faraday effect from the optical windows of the cryostat was subtracted from the experimental data using the same measurement procedure on a nonmagnetic mirror. All MOKE measurements were performed upon cooling and heating with no noticeable temperature hysteresis.

C. Theory

We calculate the MOKE spectra using noncollinear spin polarized DFT and linear response theory. In contrast to our earlier work [12] and Ref. [35], we have not used the projection on maximally localized Wannier functions here to evaluate the linear response of the systems. Instead, we followed the approach of Ref. [34] and use VASP itself to evaluate the elements of the permittivity tensor (which is a counterpart of the optical conductivity tensor).

The Kerr rotation and ellipticity in the polar configuration in the approximation of a semi-infinite medium are related to the permittivity as follows:

$$\theta_K + i\eta_K \approx \frac{-\varepsilon_{xy}}{(\varepsilon_0 - 1)\sqrt{\varepsilon_0}},$$

where $\varepsilon_0 = (\varepsilon_{xx} + \varepsilon_{yy})/2$. This approximation is justifiable because of relatively thick samples (100 nm) and their metallic behavior. This ensures the light is absorbed within the layer and is not reaching the bottom of the layer.

The projector augmented wave method as implemented in the VASP code [40] was used, where the exchange correlation functional is formulated in the generalized gradient approximation (GGA) as parameterized by Perdew–Burke–Ernzerhof [41]. Our results were obtained using a $20 \times 20 \times 20$ k-mesh sampling and a 500-eV energy cutoff to guarantee good convergence. The valence configurations of manganese, nickel, and nitrogen, are $3d^6 4s^1$, $3d^8 4s^2$, and $2s^2 2p^3$, respectively.

The intra-atomic Coulomb interaction within GGA was modified through the rotationally invariant approach to GGA + U proposed by Dudarev *et al.* [42], with Hubbard parameter, U, varying from 0 eV to 1.2 eV for the manganese site, orbital d. Supplemental Material Figures S1 and S2 [33] show the variation of the MOKE spectra with U, and Supplemental Material Figure S3 [33] shows the increase of the size of the local moments with U. In our previous DFT studies [12,23,29,43], we used $U = 0$ for simplicity. However, the availability of rich experimental data (MOKE spectra) in this study allows us to take the electronic correlations into account and identify the most suitable value of U, which we plan to use in our future simulations.

The simulations assume the same c/a ratio as observed in our film experimentally [30]. However, the lattice parameters a and c are rescaled according to the equilibrium lattice parameter obtained by VASP to $a = 0.3839$ nm and $c = 0.3846$ nm.

Finally, we note that we use Gaussian smearing to treat the partial occupancies in k-space integration with a small value of smearing, $\sigma = 0.01$ eV, which provides us with a detailed view of the Kerr spectra on output.

III. RESULTS

An epitaxial (001)-oriented Mn_3NiN thin film, of thickness 100 nm, was grown using pulsed laser deposition at 400 °C on a 10-mm × 10-mm × 0.5-mm single crystal (001)–oriented $BaTiO_3$ substrate, as detailed earlier and also described elsewhere [24]. The c and a lattice parameters of the film were measured using neutron diffraction as $c = 3.894$ Å and $a = 3.887$ Å, giving a compressive in-plane biaxial strain of $\varepsilon = -0.07\%$ [30]. In that work we observed that films grown with compressive strain appeared to support a large AHE above T_N. The neutron diffraction data confirmed that the phase above T_N had long-range magnetic order, although the magnetic structure could not be uniquely refined.

Initial characterization of the magnetic and electrical properties of the 100-nm Mn_3NiN film under investigation is shown in Fig. 1. The Néel temperature, $T_N = 240$ K, is determined from the zero-field–cooled (ZFC) magnetization shown in Fig. 1(a). The magnetization-field loops shown in Figs. 1(c–e) at 300 K, 210 K, and 170 K, respectively, show that, on cooling, the film transitions from an isotropic soft FIM phase present above T_N to the AFM Γ^{4g} phase with a large coercive field H_c. The small finite magnetization in the AFM Γ^{4g} phase originates from strain-induced canting of the local moments, creating a net moment in the [112]-type directions. In the AFM Γ^{5g} phase, this strain-induced moment is oriented along [110], so measurement of the in-plane and out-of-plane moment may give a broad indication of the magnetic state. Indeed, the in-plane and out-of-plane H_c and saturation magnetization become increasingly different as the film is cooled below T_N—indicative of the transition from FIM to Γ^{4g}, and finally rotation of the manganese spins moving toward Γ^{5g} at the lowest temperatures. We observe that the saturated anomalous Hall resistivity (ρ_{xy}) is largest when the film is in the FIM phase and decreases monotonically as the film is cooled. The origin of this anomalous Hall is from the Berry curvature of the electronic structure, not the small net moment. However, the moment does allow the antiferromagnetic domains to be aligned in an applied magnetic field and therefore facilitates measurement. The magnitude of the longitudinal resistivity (ρ_{xx}) for films on BTO compared to films on STO as shown in Fig. 1(f) demonstrates that the films grown on BTO have an additional temperature-independent scattering contribution that increases the magnitude of ρ_{xx}. This is likely due to the presence of microscopic cracking in the film caused by the phase transitions of the BTO substrate as it is cooled [44].

The polar Kerr rotation spectrum taken at 180 K [when Mn_3NiN is in the Γ^{4g} canted AFM phase; see Fig. 2(a)] is shown in Fig. 2(c). The spectral dependence is dominated by a maximum located near 1.7 eV (labeled a) and two minima near 2 and 3.7 eV (labeled b and c, respectively). At c, it reaches a maximum absolute value of 12.5 mdeg. Other smaller spectroscopic structures are visible across the spectrum. To aid interpretation of the experimental data, we calculated the theoretical polar Kerr rotation spectrum

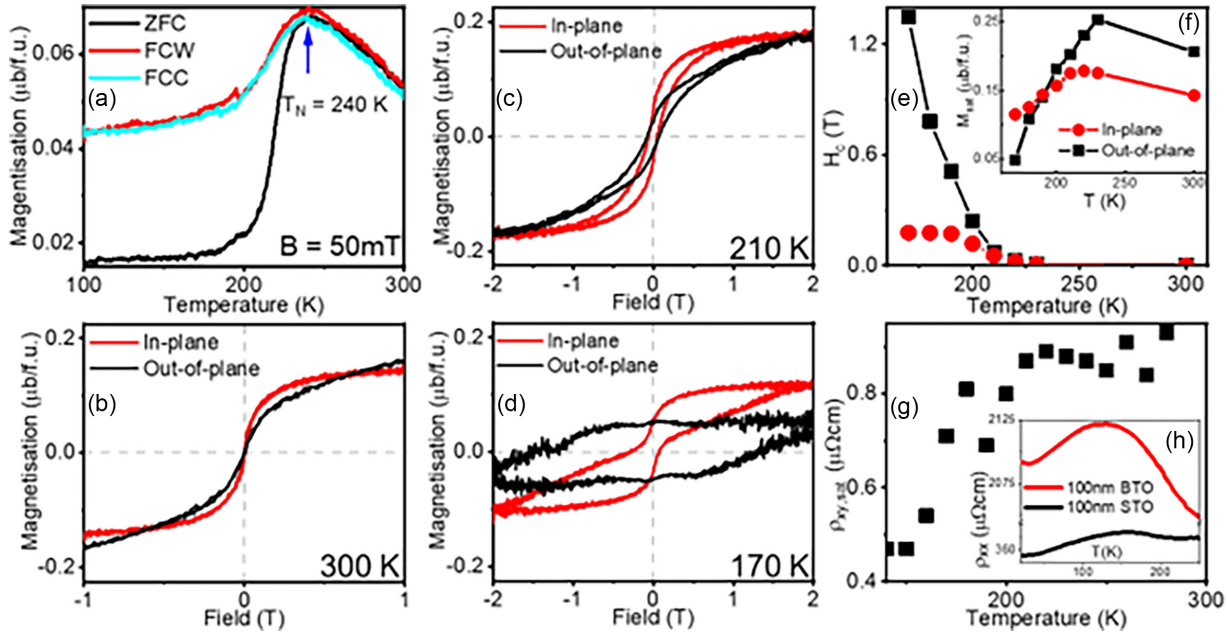

FIG. 1. (a) The antiferromagnetic transition temperature $T_N = 240$ K identified from field-cooled (measured on both warming and cooling) and zero-field–cooled $M(T)$ in 50 mT. $M(H)$ is shown in (b), (c), and (d) at 300 K, 210 K, and 170 K, respectively. (e) The coercive field $H_c(T)$ for field in the plane of the film and out of the plane and the inset (f) showing the saturation magnetization in the two field directions. (g) The saturated anomalous Hall resistivity $\rho_{xy,\mathrm{sat}}(T)$ and the inset (h) show the longitudinal resistivity $\rho_{xx}(T)$ of the Mn_3NiN film on BTO and STO substrates. $\rho_{xy,\mathrm{sat}}(T)$ is obtained by subtracting the ordinary Hall contribution.

using an *ab initio* approach (described earlier), including a smearing parameter of 0.01 eV, and the result is displayed as a black line in Fig. 2(d). Comparing the initial calculated spectrum with experimental results, the spectral behavior has some similarities but is shifted toward lower energies.

It has been previously shown that in some collinear antiferromagnets, such as CuMnAs, one can improve the DFT

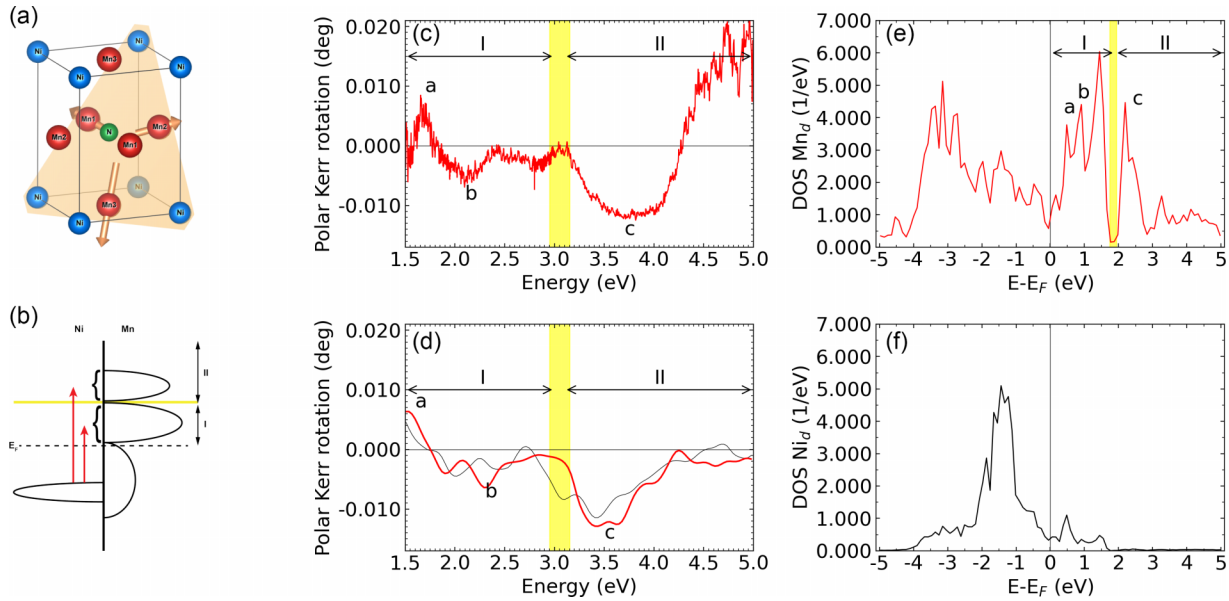

FIG. 2. (a) Schematic picture of the unit cell of Mn_3NiN together with the manganese magnetic moment alignment in the noncollinear AFM phase. (b) Simplified picture of the magneto-optically active charge transfer electronic transitions from nickel to manganese 3*d* states. The arrows with the curly backets represent groups of transitions for I and II energy regions observed in manganese density of states (DOS). (c) Experimental spectra of polar MOKE rotation taken at 180 K, obtained from field-cooled measurements in ±200 mT. The yellow region is the position of the gap-like feature in manganese DOS taken from nickel states. (d) *Ab initio* calculated polar MOKE spectrum for the AFM phase and $U = 0$ (black line) and 0.7 eV (red line); theory is multiplied by 0.1. (e) Element-resolved DOS for manganese 3*d* states with a marked gap-like feature. (f) Element-resolved DOS for nickel 3*d* states.

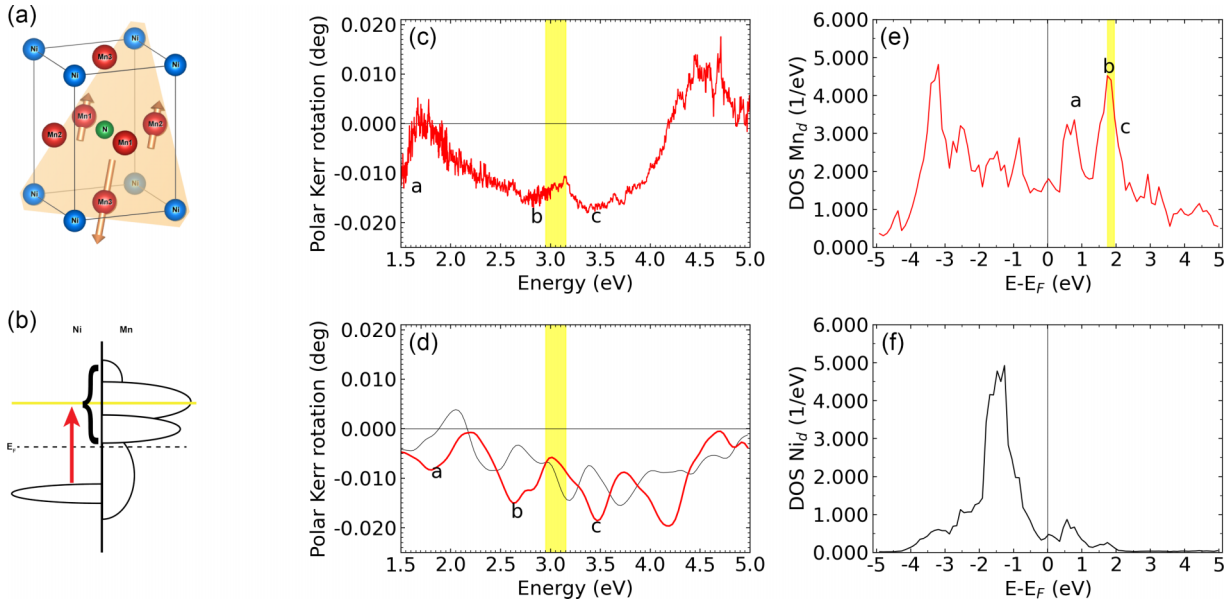

FIG. 3. (a) Schematic picture of the unit cell of Mn_3NiN together with the manganese magnetic moment alignment in the FIM phase. (b) Simplified picture of the magneto-optically active charge transfer electronic transitions from nickel to manganese 3*d* states. The arrow with the curly backet represents all transitions for the whole investigated energy region. (c) Experimental spectra of polar MOKE rotation taken at 300 K, obtained from data taken at ±200 mT. The yellow region is the position of the gap-like feature in manganese DOS of the AFM phase taken from nickel states. (d) *Ab initio* calculated polar MOKE spectrum for the FIM phase and $U = 0$ (black line) and 0.7 eV (red line); theory is multiplied by 0.1. (e) Element-resolved DOS for manganese 3*d* states with marked gap-like feature in the AFM phase. (f) Element-resolved DOS for nickel 3*d* states.

description of the electronic structure by including the onsite Coulomb repulsion using Hubbard parameter U on manganese 3*d* orbitals [45]. This repulsion lifts the unoccupied manganese *d* states further away from the Fermi level, resulting in a blueshift in the optical and magneto-optical responses. We have calculated several theoretical spectra of the polar Kerr rotation with U values varying from 0 to 1.2 eV (see Supplemental Material Figures S1 and S2 [33]). We observe a remarkable agreement of the measured and simulated spectra within a narrow range of U values around $U = 0.7$ eV. The corresponding Kerr rotation spectrum is displayed in Fig. 2(d) by a red line. All spectral structures (*a*–*c*) in the experimental spectrum were observed in the theoretical spectrum at similar energies. The most prominent feature, the sharp increase in the magnitude of the Kerr rotation at 3.2 eV, coincides with the simulated feature for $U = 0.7$ eV. It has to be noted that the amplitude of the theoretical spectrum had to be divided by a factor of 10 to match the amplitude of the experiment, in agreement with what has been previously found for AHE [12]. This discrepancy can be explained in part by finite temperature and inhomogeneous broadening due to the lack of perfect crystallinity of the films.

We investigated the magneto-optical response in the FIM phase [shown schematically in Fig. 3(a)] by measuring the polar Kerr rotation at room temperature; the resulting spectrum is displayed in Fig. 3(c). The spectrum is significantly different from the spectrum in the noncollinear AFM phase and shows less prominent spectral structures. A local minimum is present near 1.6 eV (labeled as *a*); otherwise, the spectral behavior is smooth, with two minima near 2.8 and 3.5 eV (labeled *b* and *c*, respectively). At *c*, the Kerr angle reaches a maximum absolute value of 18 mdeg.

To understand the origin of the changes in polar Kerr rotation upon the transformation to the FIM phase, we again calculated the theoretical spectral dependence for $U = 0$ eV and for $U = 0.7$ eV from first principles, and the results are shown in Fig. 3(d). It is still possible to map the observed spectral peaks to the experimental spectrum, but the agreement is notably lower than in the noncollinear AFM phase. We propose two main causes for this: (i) thermal broadening of the transition peaks (the calculations are performed for $T = 0$ K) and (ii) uncertainty in the direction and magnitude of the magnetic moments, which is challenging to measure in thin films and no similar phase exists in unstrained bulks for comparison. However, the energies of all observed structures, except *a*, are still in reasonable agreement.

IV. DISCUSSION

In the AFM phase, the magnitude of the Kerr angle (12.5 mdeg) is in the same order as previously reported in bulk Mn_3Sn (20 mdeg) [21], and the spectral dependence of polar Kerr rotation resembles that measured in other compounds containing manganese atoms, such Ni-Mn-Ga [46,47] or $La_{2/3}Sr_{1/3}MnO_3$ [48–50]. This suggests that the localized 3*d* electrons of manganese are mainly responsible for the magneto-optical response in the investigated samples. In the FIM phase, the maximal absolute amplitude of 18 mdeg at 3.4 eV is even larger than the noncollinear AFM phase [Fig. 3(c)], and the ratio of the Kerr angle to the magnetic

TABLE I. A comparison of the anomalous Hall effects present in a variety of magnetic materials. The strength of the AHE relative to the magnetization of the material is parametrized by the ratio column.

Material	Magnetic ordering	MOKE amplitude (mdeg)	Magnetization (μ_B/f.u.)	Ratio	Origin	Reference
Mn_3NiN (100 nm on BTO) at 300 K	FIM	18	0.08	225	This work	This work
Y_3Fe_5O	FM	150	5	30	Theory	[56]
Bi_3Fe_5O	FM	1100	4.4	250	Theory	[56]
CoPt	FM	500–1000	2.2	227	Theory + exp.	[57]
Fe_3GeTe_2	FM	1000–3000	6.3	159	Theory	[58]
AuMnSb	FM	700	4.2	167	Theory + exp.	[59]
PtMnSb	FM	1800	3.97	453	Theory + exp.	[60]
Mn_3Sn (bulk)	AFM	20	0.005	4000	Exp.	[21]
NiMnSb	FM	1200	3.85	312	Exp.	[60]

moment is comparable or larger to other well-known ferrimagnets, as shown in Table I.

To link qualitatively the magneto-optical response of the investigated sample with its electronic structure, the element-resolved DOS for the 3*d* orbitals of nickel and manganese were calculated and are plotted in Fig. 2(e) and 2(f) for the AFM phase, and Fig. 3(e) and 3(f) for the FIM phase. The *s* and *p* DOS are small and too far from the Fermi energy to play an important role in the visible magneto-optical response. Figures 2(f) and 3(f) clearly show a relatively narrow nickel band in the DOS around 1.4 and 1.3 eV below the Fermi energy, while there are almost no states above the Fermi energy. This indicates that the excited states of the electronic transitions, which are responsible for the magneto-optical response, may be of manganese origin. Indeed, the DOS of manganese electrons are more complicated, with rich energy dependence above the Fermi level, as follows from Figs. 2(e) and 3(e). In the AFM phase, there is a gap-like feature above the Fermi energy, from approximately 1.7 to 1.9 eV [marked as yellow in Figs. 2(e) and 3(e)]. This separates the DOS into two distinct energy regions [marked as I and II in Figs. 2(b)–2(e)]. Taking the ground state as 3*d* nickel, we can assign all spectral structures seen in the experimental and theoretical spectra to the prominent peaks in the DOS that match in energy, as shown in Fig. 2(e). We can therefore infer that the magneto-optical response of Mn_3NiN in the AFM phase is primarily driven by 3*d* nickel-to-manganese charge transfer electron transitions, as schematically shown in Fig. 2(b).

Comparing the DOS of the noncollinear AFM phase [shown in Figs. 2(e) and 2(f)] to the FIM phase [shown in Fig. 3(e) and 3(f)], there is very little difference between the nickel states but large differences between the manganese DOS. This is as expected, since only the manganese magnetic moment alignment is different in both phases. There is clearly a rearrangement of valence electronic states from Γ^{4g} to FIM. The gap-like feature, highlighted in yellow, has completely disappeared in the FIM phase and, instead, there is a large band in the manganese DOS 1.9 eV above the Fermi energy. This is a clear origin of some of the differences between the polar Kerr rotation spectra of the FIM and AFM phases. Focusing now on the FIM phase, we identified two prominent bands in the manganese DOS above the Fermi energy as correlating to the spectral features *a* and *b* present in both the experimental data and theoretical calculations [Fig. 3(c) and 3(d)]. These bands are likely to be considerably broadened at room temperature, giving a smoother magneto-optical response than zero-temperature calculations predict. The schematic diagram of the transition mechanism in the FIM phase is shown in Fig. 3(b).

Since the Mn_3NiN noncollinear AFM and FIM phases can be clearly identified from the magneto-optical response, we have measured the temperature dependence of the polar Kerr rotation spectra across the transition from 180 K to 270 K. The temperature evolution of the spectra is shown in Fig. 4(b). From the figure, one can see that notable changes in the spectra with temperature occur within the spectral range from 2 to 4 eV, reaching their maxima in the vicinity of 3eV, which is consistent with our previous discussion. This is made even clearer by observing the difference spectrum between 180 K and 300 K in Fig. 4(c), with the gap region highlighted in yellow.

The change in the magneto-optical response occurs within a relatively broad temperature range, indicating a gradual transformation of the samples' surface from the noncollinear AFM to the FIM phase upon heating. As the incident light has a spot size that is 2 mm in diameter, the MOKE spectrum carries integral information over a large region of the film. In collinear antiferromagnets, previous reports have indicated that the transition across the Néel temperature results in a non-homogeneous magnetic order in the sample, before reaching the single magnetic phase [51]. We therefore took an intermediate polar Kerr rotation spectrum at 210 K and calculated the theoretical spectrum, assuming a phase mixture of 40% FIM and 60% noncollinear AFM. The result is shown in Fig. 4(d), where the calculated mixed spectrum has good agreement with the experimental data. Further investigation of the transition in the future would be facilitated using a scanning MOKE microscope with a focused beam of light (energy, 3eV), which could laterally resolve the magnetic order in the sample.

It is well understood that the intrinsic AHC σ_{xy} is proportional to the integrated Berry phase curvature across the Brillouin zone, while the magnitude of the MOKE signal relates to both the magnitude of the Berry phase curvature and the specific allowed optical transitions. In Mn_3NiN, the

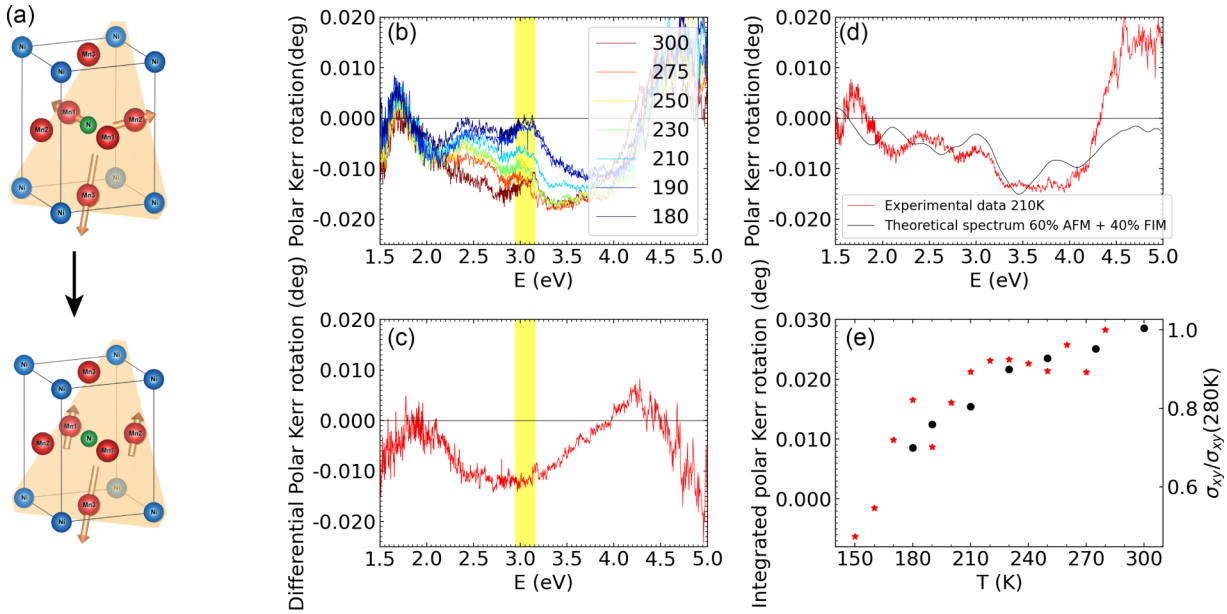

FIG. 4. (a) Schematic picture of the unit cell of Mn_3NiN together with the manganese magnetic moment alignment across the transition from the AFM to FIM phase induced by the change of temperature. (b) Temperature evolution of experimental spectra of polar MOKE rotation, obtained from data taken at ±200 mT. The yellow region is the position of the gap-like feature in the manganese DOS of the AFM phase taken from nickel states. (c) Differential MOKE spectrum at 300 K to 180 K with marked position of the gap-like feature in the manganese DOS of the AFM phase. (d) Experimental MOKE spectrum taken at 210 K together with theoretical calculation when taking into account 60% of the AFM and 40% of the FIM phase; theory is multiplied by 0.1. (e) A comparison of the temperature evolution of AHE conductivity (red stars) and integrated MOKE (black circles) between 1.5 and 4.3 eV.

maximum MOKE and AHE signals are both found in the FIM phase that survives robustly at room temperature. The Berry curvature is also predicted to be a factor of two higher in the FIM phase due to the changes in band structure. Figure 4(e) shows the direct comparison between the temperature dependence of the integrated MOKE spectra (in the spectral range from 1.5 to 4.3 eV) and σ_{xy}, with striking similarity. Clearly the temperature dependence of the Berry phase—which is predicted and found to be maximal in the FIM phase and zero in the Γ^{5g} AFM phase—dominates the temperature dependence of both phenomena.

V. CONCLUSION

In this study we use MOKE theoretical analysis and experimentation to confirm the magnetic space group of the high-temperature FIM phase of Mn_3NiN thin film on BTO. We show that the intrinsic properties of the band structure (nonzero Berry curvature) dominates the large MOKE response in the soft ferrimagnetic phase at room temperature. The material family overall demonstrates large magneto-optical signals and an anomalous Hall effect, and very early steps in piezoelectric control of the AFM phase have recently been demonstrated [52]. A magnetic symmetry-driven FIM phase that may support fast magnetization dynamics has wide-ranging implications for spintronic application as well as, for example, high-frequency magneto-optical spatial light modulations [53].The work is also timely in light of the recent classification of magnetic materials, named "altermagnets," that are also collinear spin systems, and like the ferrimagnetic phase studied here, show the AHE without strong relativistic effects [54,55].

ACKNOWLEDGMENTS

We acknowledge fruitful discussions with Jakub Železný and Joerg Wunderlich.

This work was supported in part by the Ministry of Education, Youth and Sports of the Czech Republic from the OP RDE programme (Project No. MATFUN CZ.02.1.01/0.0/0.0/15_003/0000487) and the Czech grant agency (Grants No. 19–09882S and No. 22–21974S). J. Z. acknowledges support from Charles University (Grant No. PRIMUS/20/SCI/018). The work of J. Z. was supported by the Ministry of Education, Youth and Sports of the Czech Republic from the OP RDE programme under the project International Mobility of Researchers MSCAIF at CTU (No. CZ.02.2.69/0.0/0.0/18 070/0010457) and through the e-INFRA CZ (ID No. 90140). F. J acknowledges funding from Hitachi Cambridge, and F. J. and L. F. C. from the UK Engineering and Physical Sciences Research Council. D.B. is grateful for support from a Leverhulme Trust Early Career Fellowship (No. ECF-2019-351) and a University of Glasgow Lord Kelvin Adam Smith Fellowship.

[1] T. Jungwirth, X. Marti, P. Wadley, and J. Wunderlich, Antiferromagnetic spintronics, Nat. Nanotechnol. **11**, 231 (2016).

[2] J. Železný, P. Wadley, K. Olejník, A. Hoffmann, and H. Ohno, Spin transport and spin torque in antiferromagnetic devices, Nat. Phys. **14**, 220 (2018).

[3] P. Wadley *et al.*, Electrical switching of an antiferromagnet, Science **351**, 587 (2016).

[4] P. Wadley, S. Reimers, M. J. Grzybowski, C. Andrews, M. Wang, J. S. Chauhan, B. L. Gallagher, R. P. Campion, K. W. Edmonds, S. S. Dhesi, F. Maccherozzi, V. Novak, J. Wunderlich, and T. Jungwirth, Current polarity-dependent manipulation of antiferromagnetic domains, Nat. Nanotechnol. **13**, 362 (2018).

[5] V. M. T. S. Barthem, C. V. Colin, H. Mayaffre, M. H. Julien, and D. Givord, Revealing the properties of Mn_2Au for antiferromagnetic spintronics, Nat. Commun. **4**, 2892 (2013).

[6] S. Y. Bodnar, L. Šmejkal, I. Turek, T. Jungwirth, O. Gomonay, J. Sinova, A. A. Sapozhnik, H. J. Elmers, M. Kläui, and M. Jourdan, Writing and reading antiferromagnetic Mn_2Au by Néel spin-orbit torques and large anisotropic magnetoresistance, Nat. Commun. **9**, 348 (2018).

[7] M. Wang *et al.*, Spin flop and crystalline anisotropic magnetoresistance in CuMnAs, Phys. Rev. B **101**, 094429 (2020).

[8] O. J. Amin, K. W. Edmonds, and P. Wadley, Electrical control of antiferromagnets for the next generation of computing technology, Appl. Phys. Lett. **117**, 010501 (2020).

[9] A. K. Nayak, J. E. Fischer, Y. Sun, B. Yan, J. Karel, A. C. Komarek, C. Shekhar, N. Kumar, W. Schnelle, J. Kübler, C. Felser, and S. S. P. Parkin, Large anomalous Hall effect driven by a nonvanishing Berry curvature in the noncolinear antiferromagnet Mn_3Ge, Sci. Adv. **2**, e1501870 (2016).

[10] H. Chen, Q. Niu, and A. H. MacDonald, Anomalous Hall effect arising from noncollinear antiferromagnetism, Phys. Rev. Lett. **112**, 017205 (2014).

[11] S. Nakatsuji, N. Kiyohara, and T. Higo, Large anomalous Hall effect in a non-collinear antiferromagnet at room temperature, Nature (London) **527**, 212 (2015).

[12] D. Boldrin, I. Samathrakis, J. Zemen, A. Mihai, B. Zou, F. Johnson, B. D. Esser, D. W. McComb, P. K. Petrov, H. Zhang, and L. F. Cohen, Anomalous Hall effect in noncollinear antiferromagnetic Mn_3NiN thin films, Phys. Rev. Mater. **3**, 094409 (2019).

[13] Y. You, H. Bai, X. Chen, Y. Zhou, X. Zhou, F. Pan, and C. Song, Room temperature anomalous Hall effect in antiferromagnetic Mn3SnN films, Appl. Phys. Lett. **117**, 222404 (2020).

[14] G. Gurung, D.- F. Shao, T. R. Paudel, and E. Y. Tsymbal, Anomalous Hall conductivity of noncollinear magnetic antiperovskites, Phys. Rev. Mater. **3**, 044409 (2019).

[15] T. Higo, D. Qu, Y. Li, C. L. Chien, Y. Otani, and S. Nakatsuji, Anomalous Hall effect in thin films of the Weyl antiferromagnet Mn_3Sn, Appl. Phys. Lett. **113**, 202402 (2018).

[16] J. Yan, X. Luo, H. Y. Lv, Y. Sun, P. Tong, W. J. Lu, X. B. Zhu, W. H. Song, and Y. P. Sun, Room-temperature angular-dependent topological Hall effect in chiral antiferromagnetic Weyl semimetal Mn_3Sn, Appl. Phys. Lett. **115**, 102404 (2019).

[17] M. Ikhlas, T. Tomita, T. Koretsune, M.- T. Suzuki, D. Nishio-Hamane, R. Arita, Y. Otani, and S. Nakatsuji, Large anomalous Nernst effect at room temperature in a chiral antiferromagnet, Nat. Phys. **13**, 1085 (2017).

[18] H. Reichlova, T. Janda, J. Godinho, A. Markou, D. Kriegner, R. Schlitz, J. Zelezny, Z. Soban, M. Bejarano, H. Schultheiss, P. Nemec, T. Jungwirth, C. Felser, J. Wunderlich, and S. T. B. Goennenwein, Imaging and writing magnetic domains in the non-collinear antiferromagnet Mn_3Sn, Nat. Commun. **10**, 5459 (2019).

[19] H. Narita, T. Higo, M. Ikhlas, S. Nakatsuji, and Y. Otani, Effect of sample size on anomalous Nernst effect in chiral antiferromagnetic Mn_3Sn devices, Appl. Phys. Lett. **116**, 072404 (2020).

[20] F. Johnson, J. Kimák, J. Zemen, Z. Šobáň, E. Schmoranzerová, J. Godinho, P. Němec, S. Beckert, H. Reichlová, D. Boldrin, and J. Wunderlich, Identifying the Octupole Antiferromagnetic Domain Orientation in Mn_3NiN by Scanning Anomalous Nernst Effect Microscopy, Appl. Phys. Lett. **120**, 232402 (2022).

[21] T. Higo, H. Man, D. B. Gopman, L. Wu, T. Koretsune, O. M. J. van't Erve, Y. P. Kabanov, D. Rees, Y. Li, M.-T. Suzuki, S. Patankar, M. Ikhlas, C. L. Chien, R. Arita, R. D. Shull, J. Orenstein, and S. Nakatsuji, Large magneto-optical Kerr effect and imaging of magnetic octupole domains in an antiferromagnetic metal, Nat. Photonics **12**, 73 (2018).

[22] P. Lukashev, R. F. Sabirianov, and K. Belashchenko, Theory of the piezomagnetic effect in Mn-based antiperovskites, Phys. Rev. B **78**, 184414 (2008).

[23] J. Zemen, Z. Gercsi, and K. G. Sandeman, Piezomagnetism as a counterpart of the magnetovolume effect in magnetically frustrated Mn-based antiperovskite nitrides, Phys. Rev. B **96**, 024451 (2017).

[24] D. Boldrin, A. P. Mihai, B. Zou, J. Zemen, R. Thompson, E. Ware, B. V. Neamtu, L. Ghivelder, B. Esser, D. W. McComb, P. Petrov, and L. F. Cohen, Giant piezomagnetism in Mn_3NiN, ACS Appl. Mater. Interfaces **10**, 18863 (2018).

[25] Z. Q. Liu, H. Chen, J. M. Wang, J. H. Liu, K. Wang, Z. X. Feng, H. Yan, X. R. Wang, C. B. Jiang, J. M. D. Coey, and A. H. MacDonald, Electrical switching of the topological anomalous Hall effect in a non-collinear antiferromagnet above room temperature, Nat. Electron. **1**, 172 (2018).

[26] H. Guo, Z. Feng, H. Yan, J. Liu, J. Zhang, X. Zhou, P. Qin, J. Cai, Z. Zeng, X. Zhang, X. Wang, H. Chen, H. Wu, C. Jiang, and Z. Liu., Giant piezospintronic effect in a noncollinear antiferromagnetic metal, Adv. Mater. **32**, 2002300 (2020).

[27] H. Yan, Z. Feng, S. Shang, X. Wang, Z. Hu, J. Wang, Z. Zhu, H. Wang, Z. Chen, H. Hua, W. Lu, J. Wang, P. Qin, H. Guo, X. Zhou, Z. Leng, Z. Liu, C. Jiang, M. Coey, and Z. Liu, A piezoelectric, strain-controlled antiferromagnetic memory insensitive to magnetic fields, Nat. Nanotechnol. **14**, 131 (2019).

[28] J. Finley and L. Liu, Spintronics with compensated ferrimagnets, Appl. Phys. Lett. **116**, 110501 (2020).

[29] J. Zemen, E. Mendive-Tapia, Z. Gercsi, R. Banerjee, J. B. Staunton, and K. G. Sandeman, Frustrated magnetism and caloric effects in Mn-based antiperovskite nitrides: Ab initio theory, Phys. Rev. B **95**, 184438 (2017).

[30] D. Boldrin, F. Johnson, R. Thompson, A. P. Mihai, B. Zou, J. Zemen, J. Griffiths, P. Gubeljak, K. L. Ormandy, P. Manuel, D. D. Khalyavin, B. Ouladdiaf, N. Qureshi, P. Petrov, W. Branford, and L. F. Cohen, The biaxial strain dependence of magnetic order in spin frustrated Mn3NiN thin films, Adv. Funct. Mater. **29**, 1902502 (2019).

[31] H. T. Stokes, D. M. Hatch, and B. J. Campbell, FINDSYM, ISOTROPY Software Suite, iso.byu.edu.

[32] H. T. Stokes and D. M. Hatch, FINDSYM: Program for identifying the space-group symmetry of a crystal, J. Appl. Crystallogr. **38**, 237 (2005).

[33] See Supplemental Material at http://link.aps.org/supplemental/10.1103/PhysRevB.107.014404 for a summary of the magnetic phases and details on the effect of the Hubbard parameter U on calculations.

[34] W. Feng, G.- Y. Guo, J. Zhou, Y. Yao, and Q. Niu, Large magneto-optical Kerr effect in noncollinear antiferromagnets Mn_3X (X = Rh, Ir, Pt), Phys. Rev. B **92**, 144426 (2015).

[35] X. Zhou, J.- P. Hanke, W. Feng, F. Li, G.- Y. Guo, Y. Yao, S. Blügel, and Y. Mokrousov, Spin-order dependent anomalous Hall effect and magneto-optical effect in the noncollinear antiferromagnets Mn_3XN with X = Ga, Zn, Ag, or Ni, Phys. Rev. B **99**, 104428 (2019).

[36] F. J. Kahn, P. S. Pershan, and J. P. Remeika, Ultraviolet magneto-optical properties of single-crystal orthoferrites, garnets, and other ferric oxide compounds, Phys. Rev. **186**, 891 (1969).

[37] J. Železný, Symmetr, https://bitbucket.org/zeleznyj/linear-response-symmetry.

[38] E. Krén, G. Kádár, L. Pál, J. Sólyom, P. Szabó, and T. Tarnóczi, Magnetic structures and exchange interactions in the Mn-Pt system, Phys. Rev. **171**, 574 (1968).

[39] E. Jesenská, T. Ishibashi, L. Beran, M. Pavelka, J. Hamrle, R. Antoš, J. Zázvorka, and M. Veis, Optical and magneto-optical properties of $Gd_xFe_{(100-x)}$ thin films close to the compensation point, Sci. Rep. **9**, 16547 (2019).

[40] G. Kresse and J. Hafner, Ab initio molecular dynamics for liquid metals, Phys. Rev. B **47**, 558 (1993).

[41] J. P. Perdew, K. Burke, and M. Ernzerhof, Generalized Gradient Approximation Made Simple, Phys. Rev. Lett. **77**, 3865 (1996).

[42] S. L. Dudarev, G. A. Botton, S. Y. Savrasov, C. J. Humphreys, and A. P. Sutton, Electron-energy-loss spectra and the structural stability of nickel oxide: An LSDA + U study, Phys. Rev. B **57**, 1505 (1998).

[43] H. K. Singh, I. Samathrakis, N. M. Fortunato *et al.*, Multifunctional antiperovskites driven by strong magnetostructural coupling, npj Comput. Mater. **7**, 98 (2021).

[44] Y. Bai, X. Han, X.- C. Zheng, and L. Qiao, Both high reliability and giant electrocaloric strength in BaTiO3 ceramics, Sci. Rep. **3**, 2895 (2013).

[45] M. Veis *et al.*, Band structure of CuMnAs probed by optical and photoemission spectroscopy, Phys. Rev. B **97**, 125109 (2018).

[46] M. Veis, L. Beran, M. Zahradnik, R. Antos, L. Straka, J. Kopecek, L. Fekete, and O. Heczko, Magneto-optical spectroscopy of ferromagnetic shape-memory Ni-Mn-Ga alloy, J. Appl. Phys. **115**, 17A936 (2014).

[47] S. Uba, A. Bonda, L. Uba, L. V. Bekenov, V. N. Antonov, and A. Ernst, Electronic structure and magneto-optical Kerr effect spectra of ferromagnetic shape-memory Ni-Mn-Ga alloys: Experiment and density functional theory calculations, Phys. Rev. B **94**, 054427 (2016).

[48] M. Zahradník, T. Maroutian, M. Zelený, L. Horák, G. Kurij, T. Maleček, L. Beran, Š. Višňovský, G. Agnus, P. Lecoeur, and M. Veis, Electronic structure of $La_{2/3}Sr_{1/3}MnO_3$: Interplay of oxygen octahedra rotations and epitaxial strain, Phys. Rev. B **99**, 195138 (2019).

[49] L. Uba, S. Uba, L. P. Germash, L. V. Bekenov, and V. N. Antonov, Electronic structure and magneto-optical spectra of $La_xSr_{1-x}MnO_3$ perovskites: Theory and experiment, Phys. Rev. B **85**, 125124 (2012).

[50] J. Mistrik, T. Yamaguchi, M. Veis, E. Liskova, S. Visnovsky, M. Koubaa, A. M. Haghiri-Gosnet, P. Lecoeur, J. P. Renard, W. Prellier, and B. Mercey, Magneto-optical and optical spectroscopic ellipsometries of $La_{2/3}Sr_{1/3}MnO_3$ thin films, J. Appl. Phys. **99**, 08Q317 (2006).

[51] V. Saidl, M. Brajer, L. Horák, H. Reichlová, K. Výborný, M. Veis, T. Janda, F. Trojánek, M. Maryško, I. Fina, X. Marti, T. Jungwirth, and P. Němec, Investigation of magneto-structural phase transition in FeRh by reflectivity and transmittance measurements in visible and near-infrared spectral region, New J. Phys. **18**, 083017 (2016).

[52] F. Johnson, D. Boldrin, J. Zemen, D. Pesquera, J. Kim, X. Moya, H. Zhang, H. K. Singh, I. Samathrakis, and L. F. Cohen, Strain dependence of Berry-phase-induced anomalous Hall effect in the non-collinear antiferromagnet Mn_3NiN, Appl. Phys. Lett. **119**, 222401 (2021).

[53] K. Aoshima, N. Funabashi, K. Machida, Y. Miyamoto, K. Kuga, T. Ishibashi, N. Shimidzu, and F. Sato, Submicron magneto-optical spatial light modulation device for holographic displays driven by spin-polarized electrons, J. Display Technol. **6**, 374 (2010).

[54] L. Šmejkal, J. Sinova, and T. Jungwirth, Beyond Conventional Ferromagnetism and Antiferromagnetism: A Phase with Nonrelativistic Spin and Crystal Rotation Symmetry, Phys. Rev. X **12**, 031042 (2022).

[55] L. Šmejkal, A. H. MacDonald, J. Sinova, S. Nakatsuji, and T. Jungwirth, Anomolous Hall antiferromagnets, Nat. Rev. Mater. **7**, 482 (2022).

[56] W.- K. Li and G.- Y. Guo, First-principles study on magneto-optical effects in the ferromagnetic semiconductors Y_3Fe_5O and Bi_3Fe_5O, Phys. Rev. B **103**, 014439 (2021).

[57] M. Kim, A. J. Freeman, and R. Wu, Surface effects and structural dependence of magneto-optical spectra: Ultrathin Co films and $CoPt_n$ alloys and multilayers, Phys. Rev. B **59**, 9432 (1999).

[58] M.- C. Jiang and G.- Y. Guo, Large magneto-optical effect and magnetic anisotropy energy in two-dimensional ferromagnetic metal Fe3GeTe2, Phys. Rev. B **105**, 014437 (2022).

[59] L. Offernes, P. Ravindran, and A. Kjekshus, Prediction of large polar Kerr rotation in the Heusler-related alloys AuMnSb and AuMnSn, Appl. Phys. Lett. **82**, 2862 (2003).

[60] W. Xindong, V. P. Antropov, and B. N. Harmon, First principles study of magneto-optical properties of half metallic Heusler alloys: NiMnSb and PtMnSb, IEEE Trans. Magn. **30**, 4458 (1994).